

# ABSOLUTE NODAL COORDINATE FORMULATION FOR NONLINEAR MULTIBODY MODELING OF FLARED HINGED WINGS

Keisuke Otsuka<sup>1</sup>, Chi Wing Cheng<sup>2</sup>, & Rafael Palacios<sup>2</sup>

<sup>1</sup> Tohoku University, Sendai 980-8579, Japan
<sup>2</sup>Imperial College London, London, England SW7 2AZ, United Kingdom

#### **Abstract**

The wings of transport jets are becoming high aspect ratio to reduce induced drag. Because of the high aspect ratio configuration with lightweight, the wings may undergo nonlinear large deformations induced by aerodynamic forces. To alleviate excessive large deformation under gust conditions, flared hinged wings have been developed. This study develops a new multibody simulation framework for the flared hinged wings based on absolute nodal coordinate formulation (ANCF). In this framework, the constraint equation to describe the flared hinge joint can be written in a simple linear equation. We show that the simulation results of ANCF simulation framework is in good agreement with those of a second simulation framework, namely SHARPy, based on a conventional geometrically-exact beam formulation (GEBF).

Keywords: High aspect ratio wing, Flared hinged wing, Folding wing, Aeroelasticity, Multibody dynamics

#### 1. Introduction

The wings of transport jets are becoming high aspect ratio to reduce induced drag. Because of the high aspect ratio configuration with lightweight, the wings may undergo nonlinear large deformations induced by aerodynamic forces. To alleviate excessive large deformation under gust conditions, flared hinged wings have been developed. The flared hinged wing has a folding wingtip with a slanted hinge line, as shown in Fig. 1. Multibody simulation considering geometrical nonlinearity is necessary for an accurate description of the kinematics of the flared hinged wings. However, most simulation studies of the flared hinges wings [1, 2] have used the floating frame of reference formulation (FFRF) that assumes small deformation of bodies. A geometrically nonlinear simulation framework is required for modelling high-aspect-ratio flared hinged wings.

Palacios and Cesnik [3] reviewed three major geometrically nonlinear beam formulations.

The first one is the displacement-based geometrically exact beam formulation (GEBF). This formulation uses position and rotation parameters (e.g., Euler angle, Euler parameter, or Cartesian rotation vector) as variables. Although the nonlinearity appears on both the inertia and elastic forces in 3D simulation, GEBF has been widely used in multibody simulation. Cheng et al. [4] has recently developed a multibody solver in their high-aspect-ratio-wing simulation tool, namely Simulation of High-Aspect-Ratio aeroplanes in Python (SHARPy) based on the displacement-based formulation.

The second one is the strain-based beam formulation, developed by Cesnik and Brown [5]. This formulation uses extensional strain and curvatures as variables. The nonlinearity only appears on the inertia force in this formulation. Sanghi et al. [6] extended this formulation to conduct multibody simulation and implemented in their simulation tool, namely University of Michigan/Nonlinear Aeroelastic Simulation Toolbox (UM/NAST).

The third one is the intrinsic beam formulation developed by Hodges [7]. This formulation uses internal force or moment as variables. The final form of the intrinsic formulation is a 1st-order time-differential equation. Only quadratic nonlinearity appears on the equation. Although multibody

constraint equations cannot be described by the internal variables directly, Wang and Otsuka [8] succeeded in developing a multibody simulation framework based on the intrinsic formulation.

In recent years, Otsuka et al. [9, 10] have developed a hinged wing simulation framework based on absolute nodal coordinate formulation (ANCF). ANCF was devised by Shabana [11], and then reviewed by Gerstmayr et al. [12] and Otsuka et al. [13]. ANCF uses position and gradient vectors as variables. Because these vectors are defined in the global (or absolute) coordinate system and rotation parameters (e.g., Euler angle, Euler parameter, and Cartesian rotation vector) are not used, the nonlinearity appears only on the elastic force. The linear inertia force (i.e., constant mass matrix) even in 3D simulation is an advantage of ANCF. Instead of the simple inertia force expression, ANCF is often inferior to GEBF from the viewpoint of the convergence performance with respect to number of nodal variables [14]. Otsuka et al. [15] coupled ANCF with the unsteady vortex lattice method (UVLM) [16] to analyze aeroelastic responses of high aspect ratio wings. UVLM is suitable for very flexible wings because it can calculate unsteady aerodynamic forces on lifting surfaces undergoing large motion [17]. Large aeroelastic vibrations damped by aerodynamic force were simulated by ANCF with UVLM. The simulation results were in good agreement with wind tunnel test results [18]. In addition, when the hinge line is not slanted against the free stream velocity, the accuracy of the ANCF with UVLM was experimentally validated by wind tunnel tests [9]. However, the simulation framework did not consider the slanted hinge.

There are three objectives in this study. The first objective is to develop the ANCF simulation framework that can consider the slanted hinge. The second objective is to validate the developed simulation framework by the comparison with SHARPy. The third objective is to provide benchmark simulation results that can be used for validating other geometrically nonlinear beam formulations coupled with a slanted hinge joint and/or UVLM. To achieve the third objective, we apply the ANCF simulation framework and SHARPy to a double pendulum and a high-aspect-ratio wing with relatively simple geometries.

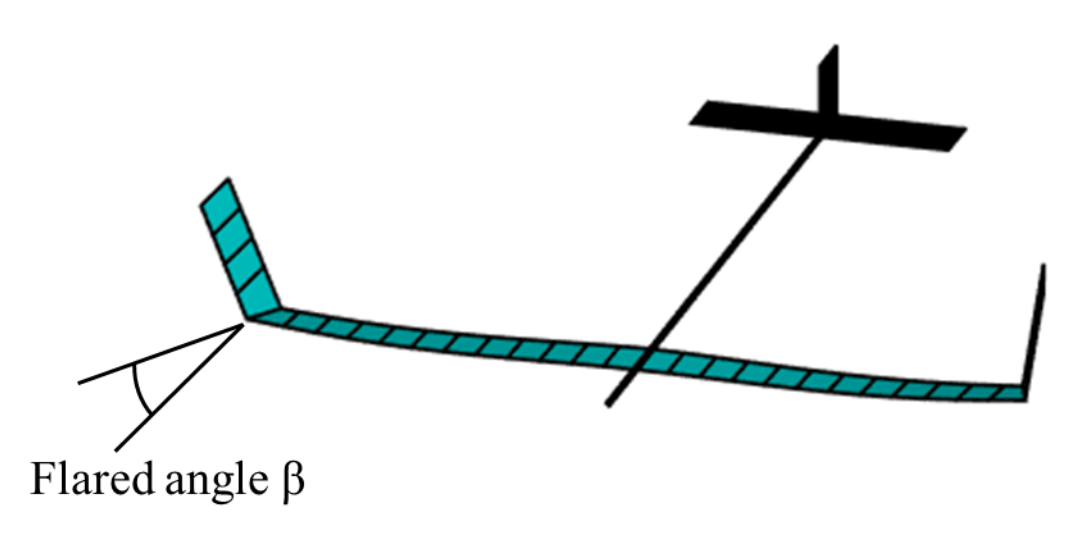


Figure 1 – Conceptual diagram of flared hinged wing.

#### 2. Absolute Nodal Coordinate Formulation (ANCF)

The 3D ANCF beam element [19] with nodes 1 and 2 is employed in the simulation framework, as shown in Fig. 2. The position vector  $\mathbf{r}$  on the element is expressed as

$$\mathbf{r} = \mathbf{S}(x, y, z)\mathbf{e}.\tag{1}$$

**S** is a shape function defined in the element coordinate system x, y, and z. **e** is a generalized nodal coordinate defined as

$$\mathbf{e} \equiv \begin{bmatrix} \left(\mathbf{r}^{1}\right)^{\mathrm{T}} & \left(\mathbf{r}_{x}^{1}\right)^{\mathrm{T}} & \left(\mathbf{r}_{y}^{1}\right)^{\mathrm{T}} & \left(\mathbf{r}_{z}^{1}\right)^{\mathrm{T}} & \left(\mathbf{r}^{2}\right)^{\mathrm{T}} & \left(\mathbf{r}_{x}^{2}\right)^{\mathrm{T}} & \left(\mathbf{r}_{z}^{2}\right)^{\mathrm{T}} \end{bmatrix}^{\mathrm{T}}.$$
 (2)

The superscripts 1 and 2 represent node numbers. The subscripts represent the position vector derivative with respect to x, y, and z. The final equation of ANCF is written in a differential algebraic equation (DAE) as

$$\mathbf{M}\ddot{\mathbf{q}} + \mathbf{F}_{\text{elastic.}} + \left(\frac{\partial \mathbf{\Phi}}{\partial \mathbf{q}}\right)^{\mathrm{T}} \lambda = \mathbf{F} \text{ and } \mathbf{\Phi} = 0,$$
 (3)

where

$$\mathbf{q} \equiv \left[ \begin{pmatrix} {}^{1}\mathbf{e}^{1} \end{pmatrix}^{\mathrm{T}} & \cdots & \left( {}^{j}\mathbf{e}^{i} \right)^{\mathrm{T}} & \cdots & \left( {}^{m}\mathbf{e}^{n} \right)^{\mathrm{T}} \right]^{\mathrm{T}}. \tag{4}$$

The superscripts i and j represent the ith node of the jth body.  $\mathbf{M}$  is a constant mass matrix.  $\mathbf{F}_{\text{elastic}}$  is a nonlinear elastic force vector.  $\lambda$  is a Lagrange multiplier.  $\mathbf{\Phi}$  is a constraint equation vector.  $\mathbf{F}$  is an external force vector.

Figure 3 shows a top view of a slanted hinge joint that connects bodies 1 and 2.  $\beta$  represents a flared angle. Owing to this slanted hinge joint, the vector  $\mathbf{a}$  on the  ${}^{1}\mathbf{r}_{x}{}^{-1}\mathbf{r}_{y}$  plane is equal to the vector  $\mathbf{b}$  on the  ${}^{2}\mathbf{r}_{x}{}^{-2}\mathbf{r}_{y}$  plane. The constraint equation of the slanted hinge joint is written as

$$\Phi = \mathbf{a} - \mathbf{b} = \mathbf{0}.$$

$$\Rightarrow \Phi = \sin \beta \begin{pmatrix} {}^{1}\mathbf{r}_{x} \end{pmatrix} + \cos \beta \begin{pmatrix} {}^{1}\mathbf{r}_{y} \end{pmatrix} - \sin \beta \begin{pmatrix} {}^{2}\mathbf{r}_{x} \end{pmatrix} - \cos \beta \begin{pmatrix} {}^{2}\mathbf{r}_{y} \end{pmatrix} = \mathbf{0}.$$
(5)

This constraint equation is linear with respect to the nodal variables in  $\bf q$ . Therefore,  $\partial \Phi/\partial \bf q$  in Eq. (3) becomes a constant matrix. This simple constraint expression is another advantage of ANCF. The linear constraint equation generates a constant velocity transformation matrix  $\bf B$ :

$$\dot{\mathbf{q}} = \frac{\partial \mathbf{q}}{\partial \mathbf{q}_{in}} \dot{\mathbf{q}}_{in} = \mathbf{B} \dot{\mathbf{q}}_{in}. \tag{6}$$

 $\mathbf{q}_{\text{in}}$  is an independent generalized coordinate vector. If this velocity transformation matrix is used, the equation of motion can be written in an ordinary differential equation (ODE) as

$$\mathbf{B}^{\mathrm{T}}\mathbf{M}\mathbf{B}\ddot{\mathbf{q}}_{\mathrm{in}} + \mathbf{B}^{\mathrm{T}}\mathbf{F}_{\mathrm{elastic.}} = \mathbf{B}^{\mathrm{T}}\mathbf{F}.$$
 (7)

In this paper, DAE in Eq. (3) rather than ODE in Eq. (7) is used.

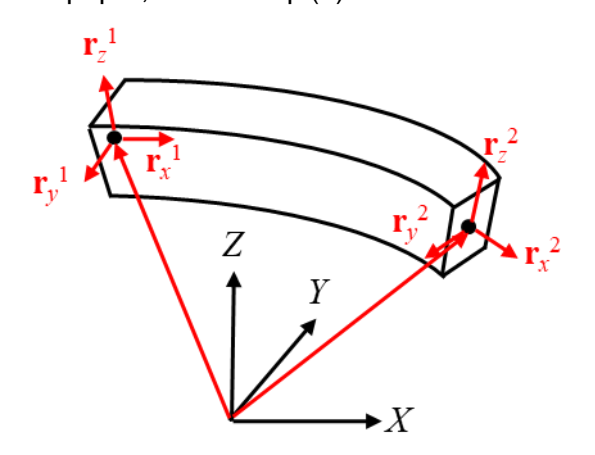


Figure 2 – ANCF beam element.

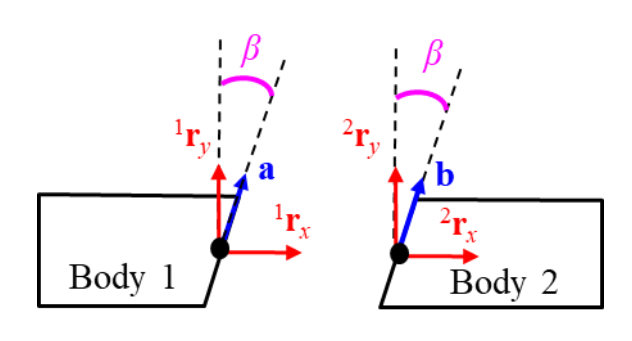


Figure 3 – Top view of slanted hinge joint.

### 3. Geometrically Exact Beam Formulation (GEBF) in SHARPy

In this section, the formulation of the multibody constraints for the hinged wing tip in SHARPy is described. The SHARPy multibody formulation make use of as many individual geometrically-exact beams as needed, coupled with Lagrange multipliers for the multibody constraints. [4, 20, 21].

As given in the reference, the general structural system of equations is described, for each generalised degree of freedom x, as

$$\begin{cases}
\mathbf{M}(\mathbf{x})\ddot{\mathbf{x}} + \mathbf{B}_{h}^{\mathsf{T}}(\mathbf{x}, t)\lambda_{h} + \mathbf{B}_{n}^{\mathsf{T}}(\dot{\mathbf{x}}, t)\dot{\lambda}_{n} &= \mathbf{f}(\mathbf{x}, \dot{\mathbf{x}}, t) = \mathbf{f}_{ext} - \mathbf{f}_{gyr} - \mathbf{f}_{stif}, \\
g_{h}(\mathbf{x}, t) &= 0, \\
g_{n}(\mathbf{x}, \dot{\mathbf{x}}, t) &= \mathbf{B}_{n}(\mathbf{x}, t) \cdot \dot{\mathbf{x}} + g_{n_{0}} = 0,
\end{cases} \tag{8}$$

in which **M** is the mass matrix and f includes the external, gyroscopic, and stiffness forces,  $g_h$  and  $g_n$  for holonomic and non-holonomic constraints,  $\mathbf{B}_h = \frac{\partial g_h}{\partial x}$  or  $\mathbf{B}_n = \frac{\partial g_n}{\partial \dot{x}}$  is the Jacobian of the constraints, and their respective Lagrange multipliers  $\lambda_h$  and  $\dot{\lambda}_n$ . In incremental form this becomes

$$\begin{bmatrix} \mathbf{M} & 0 & 0 \\ 0 & 0 & 0 \\ 0 & 0 & 0 \end{bmatrix} \begin{pmatrix} \Delta \ddot{\mathbf{x}} \\ \Delta \ddot{\lambda}_h \\ \Delta \ddot{\lambda}_n \end{pmatrix} + \begin{bmatrix} \mathbf{C} & 0 & \mathbf{B_n}^{\mathsf{T}} \\ 0 & 0 & 0 \\ \mathbf{B_n} & 0 & 0 \end{bmatrix} \begin{pmatrix} \Delta \dot{\mathbf{x}} \\ 0 \\ \Delta \dot{\lambda}_n \end{pmatrix} + \begin{bmatrix} \mathbf{K} & \mathbf{B_h}^{\mathsf{T}} & 0 \\ \mathbf{B_h} & 0 & 0 \\ 0 & 0 & 0 \end{bmatrix} \begin{pmatrix} \Delta \mathbf{x} \\ \Delta \lambda_h \end{pmatrix} = \begin{pmatrix} \mathbf{r}^{\circ} \\ -\mathbf{g}_h^{\circ} \\ -\mathbf{g}_n^{\circ} \end{pmatrix} + H.O.T., \tag{9}$$

where the tangent damping and stiffness matrices  ${\bf C}$  and  ${\bf K}$ , as well as the residual vector  ${\bf r}^\circ$  are given as

$$\begin{cases}
\mathbf{C} &= \frac{\partial \mathbf{B_n}^{\mathsf{T}} \dot{\lambda}_n}{\partial \dot{x}} - \frac{\partial \mathbf{f}}{\partial \dot{x}}, \\
\mathbf{K} &= \frac{\partial (\mathbf{M} \ddot{x})}{\partial x} + \frac{\partial \mathbf{B_n}^{\mathsf{T}} \lambda_n}{\partial x} - \frac{\partial \mathbf{f}}{\partial x}, \\
\mathbf{r}^{\circ} &= \mathbf{f} - \mathbf{M} \ddot{x} - \mathbf{B_n^{\mathsf{T}}} \lambda_n - \mathbf{B_n^{\mathsf{T}}} \dot{\lambda}_n,
\end{cases} \tag{10}$$

evaluated at the reference point. f includes the external (in this case aerodynamic as generated by the UVLM), gyroscopic, and stiffness forces. We determine **B** for the common lower pair joints that we are interested in; this formulation has been applied previously on other multibody systems such as wind turbines [21]. For a hinge connection between 2 beams, we require three and two equations for the linear and angular velocities respectively to allow only for one degree of freedom, which is the rotation about the hinge axis. They are derived next, consistent in nomenclature with [3].

#### 3.1 Definition of Reference Frames and Kinematics

Figure 4 defines the notation, used to describe the kinematics of the flexible wing with hinged wing tips. We begin from the Earth frame E in Fig. 4a, from which we define  $\mathfrak{p}(t)$  as the time-varying vector to the body-attached frame B used to track the vehicle. The rotation matrix from E to B frame  $\mathbf{R}_{BE}$  is defined with a choice of parametrisation, in this case the quaternion  $\chi^B$ . In the B frame we define  $\mathbf{r}_B^G$  as the vector to the material frame at the tip of the main wing, frame G. The rotation matrix from B to G frame  $\mathbf{R}_{GB}$  is defined, again with a choice of parametrisation, in this case the Cartesian Rotation Vector (CRV)  $\psi_B^G$ .

On the wing tip itself in Fig. 4b, separated by the hinge, we define the body-attached frame H at its root where the rotation matrix from the global frame  $\mathbf{R}_{HE}$  is a function of the quaternion  $\chi^H$ . Velocities of body-fixed frames, i.e., B and H, are given in their own FoRs respectively by  $\boldsymbol{v}_B^B$ ,  $\boldsymbol{\omega}_B^B$  and  $\boldsymbol{v}_H^H$ ,  $\boldsymbol{\omega}_H^H$ , where those at material frames, i.e. G, require a more involved formulation described further along the Section.

As the aeroelastic wing with the hinged wing tips undergoes displacements and rotations, the hinge line vector as visualised, is a function of rigid body translational and rotational movements, and flexible deformations, and almost always a function of time. Defining instead the projections of the

hinge line vector in the two local frames of reference gives  $e_H = \mathbf{R}_{HB}e_B$ , such that these vectors are now constant in time, from Euler's rotation theorem as detailed in Chapter 4.3.2 of [3].

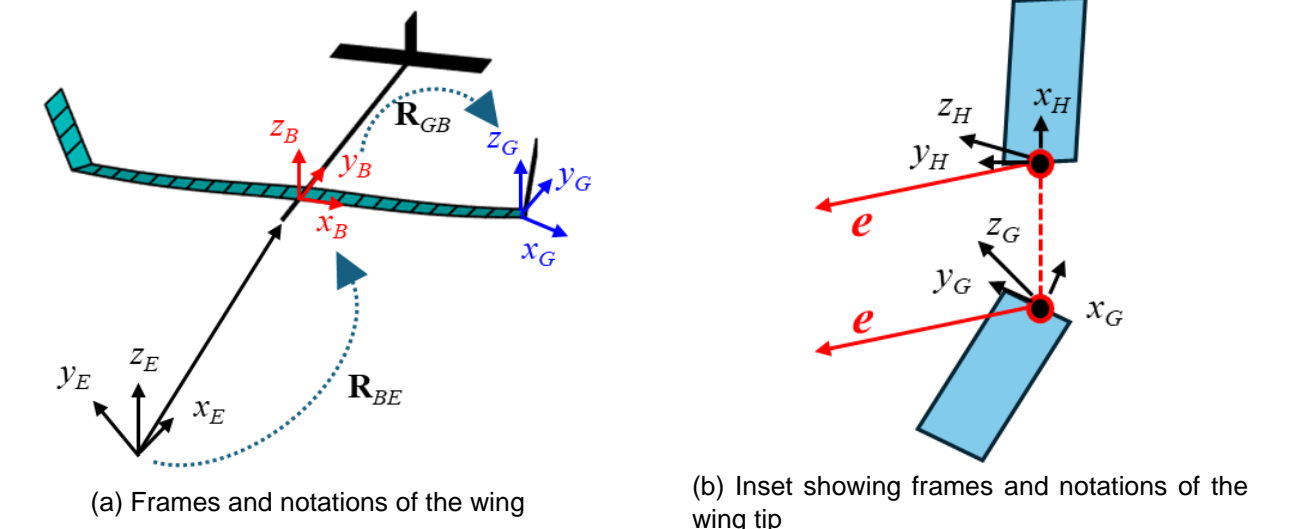


Figure 4 – Labelled quantities and frames of the flexible multibody wing assembly.

# 3.2 Linear Velocity Constraint

We begin by placing the condition of same linear velocity at frames G and H. Equating the velocities across the connection, in H frame gives

$$\boldsymbol{v}_{H}^{H} = \mathbf{R}_{HB} \cdot (\dot{\boldsymbol{r}}_{B}^{G} + \boldsymbol{v}_{B}^{B} + \widetilde{\boldsymbol{\omega}}_{B}^{B} \boldsymbol{r}_{B}^{G}), \tag{11}$$

which when written as a non-holonomic constraint in matrix form in the inertial frame E, and following the notation in Eq. (8), is

$$\boldsymbol{g}_{n1} = [-\mathbf{R}_{EB}(\chi^B) \quad -\mathbf{R}_{EB}(\chi^B) \quad \mathbf{R}_{EB}(\chi^B) \tilde{\boldsymbol{r}}_B^G \quad \mathbf{R}_{EH}(\chi^H)] \begin{bmatrix} \dot{\boldsymbol{r}}_B^G \\ \boldsymbol{v}_B^B \\ \boldsymbol{\omega}_B^H \\ \boldsymbol{v}_H^H \end{bmatrix} = \mathbf{B}_{n1}(\dot{\boldsymbol{x}}, \boldsymbol{x}, t) \dot{\boldsymbol{x}} = 0. \tag{12}$$

Apart from introducing the constraint as an extra equation in the system, we would also have to update the residual  $r^{\circ}$ , and evaluate  $\overline{\mathbf{C}}$  in Eq. (10).

#### 3.3 Angular Linear Velocity Constraint

To apply the angular velocity constraint, in practice we restrict any two pairs of corresponding points on the vectors to always have the same linear velocity. Choosing the origins of the vectors in Fig. 4b as the first pair gives Eq. (11), and additionally choosing two points along the vectors give their common linear velocity  $v_e$  in the H frame as

$$\boldsymbol{v}_{H}^{H} + \widetilde{\boldsymbol{\omega}}_{H}^{H}\boldsymbol{e}_{H} = \boldsymbol{v}_{e} = \mathbf{R}_{HB} \cdot (\dot{\boldsymbol{r}}_{B}^{G} + \boldsymbol{v}_{B}^{B} + \widetilde{\boldsymbol{\omega}}_{B}^{B}\boldsymbol{r}_{B}^{G}) + \mathbf{R}_{HG}(skew(\mathbf{T}^{GB}\dot{\boldsymbol{\psi}}_{B}^{G} + \mathbf{R}_{GB}\boldsymbol{\omega}_{B}^{B}) \cdot \boldsymbol{e}_{B}), \tag{13}$$

where T is the tangential rotational operator described in Appendix C of [3], from which we eliminate Eq. (11) to give

$$\widetilde{\boldsymbol{\omega}}_{H}^{H}\boldsymbol{e}_{H} = \mathbf{R}_{HG}(\boldsymbol{skew}(\mathbf{T}^{GB}\dot{\boldsymbol{\psi}}_{B}^{G} + \mathbf{R}_{GB}\boldsymbol{\omega}_{B}^{B}) \cdot \boldsymbol{e}_{B}), \tag{14}$$

which is transformed to G frame and recast in the form of  $g_{n2} = 0$  in matrix form,

$$\boldsymbol{g}_{n2} = \left[\tilde{e}_{B} \mathbf{R}_{GB}(\boldsymbol{\psi}_{B}^{G}) \quad \tilde{e}_{B} \mathbf{T}^{GB}(\boldsymbol{\psi}_{B}^{G}) \quad -\mathbf{R}_{GB}(\boldsymbol{\psi}_{B}^{G}) \mathbf{R}_{BE}(\boldsymbol{\chi}^{B}) \mathbf{R}_{EH}(\boldsymbol{\chi}^{H}) \tilde{e}_{H}\right] \begin{vmatrix} \boldsymbol{\omega}_{B}^{B} \\ \dot{\boldsymbol{\psi}}_{B}^{G} \\ \boldsymbol{\omega}_{H}^{H} \end{vmatrix} = \mathbf{B}_{n2}(\dot{\boldsymbol{x}}, \boldsymbol{x}, t) \dot{\boldsymbol{x}} = 0$$
 (15)

## 4. UVLM Aerodynamic Panel for Slanted Hinge Joint

The structural models are coupled with the UVLM aerodynamic model. UVLM discretizes the wing surface and wake in vortex panels with circulation  $\Gamma$  as an aerodynamic variable. The circulation is calculated by the non-penetration flow condition on wing surface and the Biot-Savart law. Then, the aerodynamic force on each panel is calculated by using the circulation as

$$\mathbf{F} = \mathbf{F}_{\text{steady}} + \mathbf{F}_{\text{unsteady}}$$

$$\equiv \sum_{i=1}^{4} (\rho \Gamma \mathbf{U}_{i} \times \delta \mathbf{l}_{i}) + \rho_{\text{air}} \frac{\partial \Gamma}{\partial t} A \mathbf{n}.$$
(16)

Here, the aerodynamic force can be divided into steady and unsteady contributions. The summation from i = 1 to i = 4 means the contributions of the four edges of the square panel.  $\rho_{air}$  is an air density. U is airflow on the edge. A is panel area.  $\mathbf{n}$  is a panel-normal vector.

Figure 5a shows the UVLM panels at the slanted hinge joint. One edge of the panels adjacent to the joint is parallel to the slanted hinge line. It should be noted that the slanted edges of the panels on both sides of the hinge line must be the same. If there is a tiny gap between the edges, numerical divergence may occur. This is because the Biot-Savart law used in UVLM causes a singularity problem when vortex edges are too close. Also, the careful choice of span-wise discretization is crucial to avoid a self-intersecting UVLM grid, as shown in Fig. 5b.

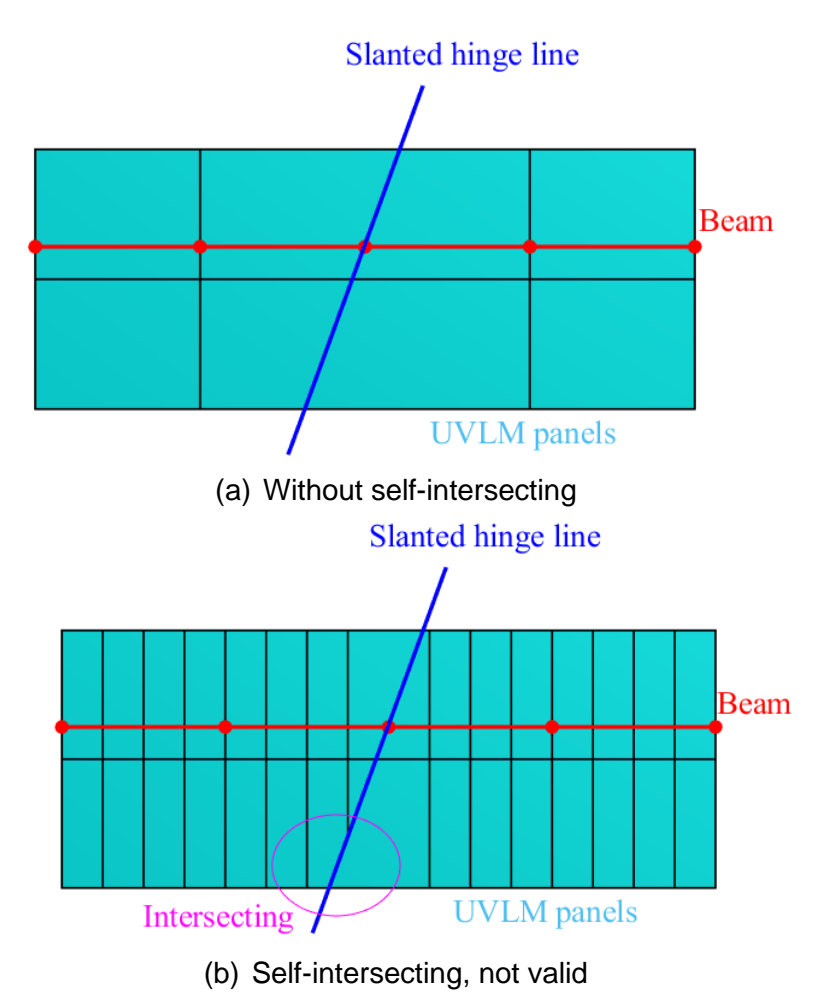


Figure 5 – UVLM panels with beam nodes near the hinge.

# 5. Multibody Simulation Results of Free-Falling Pendulum with Slanted Hinge Joint

The double pendulum problem considered by Cheng et al. [4] is simulated by the developed framework with the slanted hinge joint. Figure 6 shows the double pendulum cited from [4]. The one end of the blue body is connected to the origin of the global coordinate system with a hinge joint. The hinge line is parallel to the Y-axis. The two bodies are connected by a slanted hinge joint. Table 1 shows the parameters of each body. The two bodies have the same parameters. Table 2 shows the simulation parameters. In this section, parametric simulations with respect to the stiffness coefficient c and the flared angle  $\beta$  are conducted. Initially, the double pendulum is placed on the X-axis. The gravity in the Z-direction causes free-falling motion. The developed framework based on ANCF is compared with SHARPy. It should be noted that a fair calculation time comparison is difficult between the frameworks. This is because ANCF framework is based on MATLAB while the structural solver of SHARPy is based on Fortran. Therefore, only calculation time of the ANCF simulation framework is presented for reference. The calculation time of all ANCF simulations in this section was around 20s. The ANCF simulation was conducted by using MATLAB 2024a, CPU Ryzen Threadripper 3970X (single core), and RAM256GB.

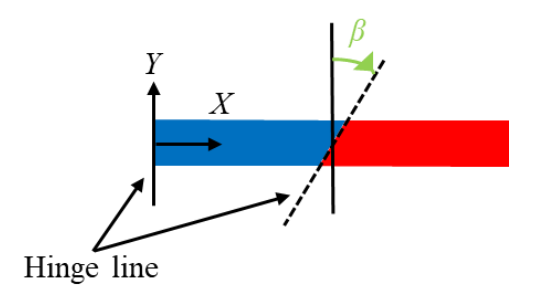


Figure 6 - Top view of double pendulum at t = 0.

Table 1 Parameters of each pendulum body

Parameters	Symbols	Values	Units
Length	L	0.50	m
Linear density	ho A	1.08	kg/m
Rotational inertia around x axis	$ ho l_{xx}$	$7.20 \times 10^{-5}$	kg × m
Rotational inertia around y axis	$ ho \mathit{l}_{\scriptscriptstyle yy}$	$3.60 \times 10^{-5}$	kg × m
Rotational inertia around z axis	$ ho l_{zz}$	$3.60 \times 10^{-5}$	kg × m
Extensional stiffness	EA	$c \times 2.80 \times 10^{5}$	N
Torsional stiffness	GJ	$c \times 6.91 \times 10^{\circ}$	$N \times m^2$
Bending stiffness around y axis	$EI_{yy}$	$c \times 9.33 \times 10^{\circ}$	$N \times m^2$
Bending stiffness around z axis	Elzz	$c \times 9.33 \times 10^{\circ}$	$N \times m^2$
Stiffness coefficient	С	1 or 0.1 or 0.01	-

Table 2 Parameters of simulation

Parameters	Symbols	Values	Units	
Simulation time	<b>t</b> end	2	S	
Time step	dt	0.002	S	
Gravity constant	g	9.8	m/s <sup>2</sup>	
Flared angle	β	0 or 45 or 90	degree	
Time integration method	Implicit generalized-α method			
Number of elements per body	5			

# 5.1 c = 1 and $\beta = 0$

Figure 7 shows the X, Y, and Z coordinates at the free end when c=1 and  $\beta=0$ . ANCF and SHARPy are in good agreement. Because of the stiffness is relatively high and zero  $\beta$ , the double pendulum can be considered as a rigid multibody system with two degrees of freedom. Therefore, two frequencies are mixed in this motion. Figure 8 shows the time history of energies calculated by ANCF. This double pendulum is a conservative system. The total energy that is a sum of the kinetic, elastic, and gravity potential energies is conserved, which shows that the developed ANCF framework satisfies energy conservation law correctly. As shown in this figure, the elastic energy is very small, this simulation result can be used for validating not only flexible but also rigid multibody simulation framework.

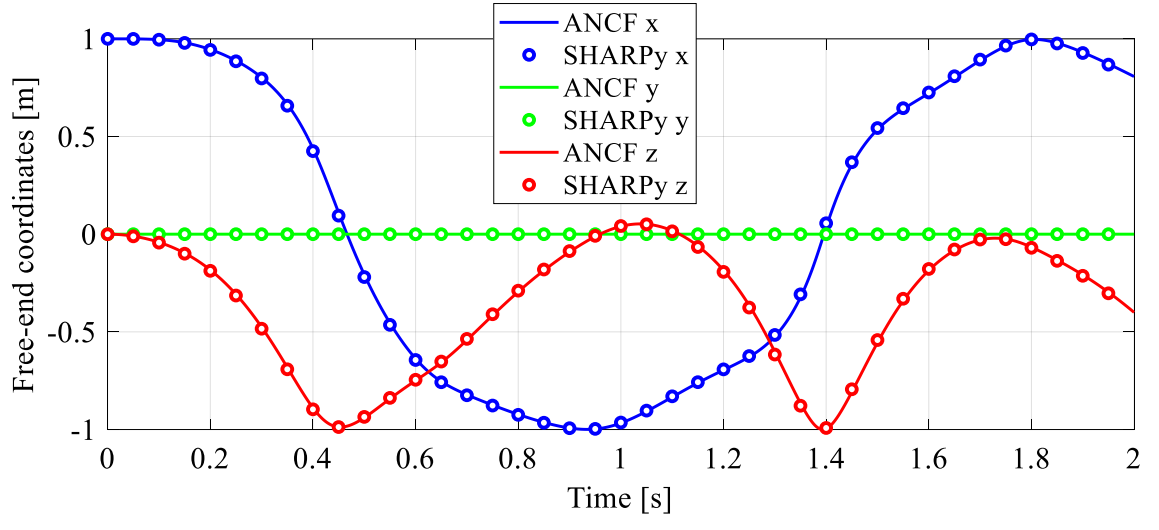


Figure 7 – Time histories of free-end coordinates of double pendulum (c = 1,  $\beta$  = 0).

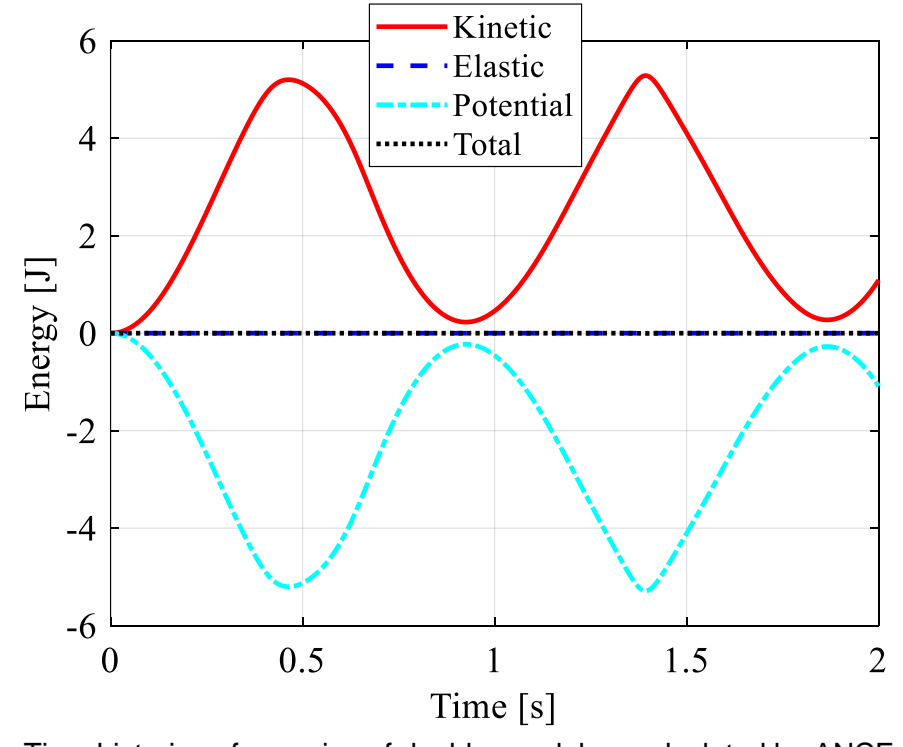


Figure 8 – Time histories of energies of double pendulum calculated by ANCF (c = 1,  $\beta$  = 0).

# 5.2 c = 1 and $\beta = 90$

Figure 9 shows the X, Y, and Z coordinates at the free end when c = 1 and  $\beta = 90$ . ANCF and SHARPy are in good agreement. Because  $\beta = 90$ , the connection of the two bodies can be considered as a rigid joint. Therefore, this double pendulum can be considered as a single pendulum with one degree of freedom. Therefore, only one frequency motion can be seen in this figure. Figure 10 shows the time histories of the energies calculated by ANCF. The total is conserved correctly.

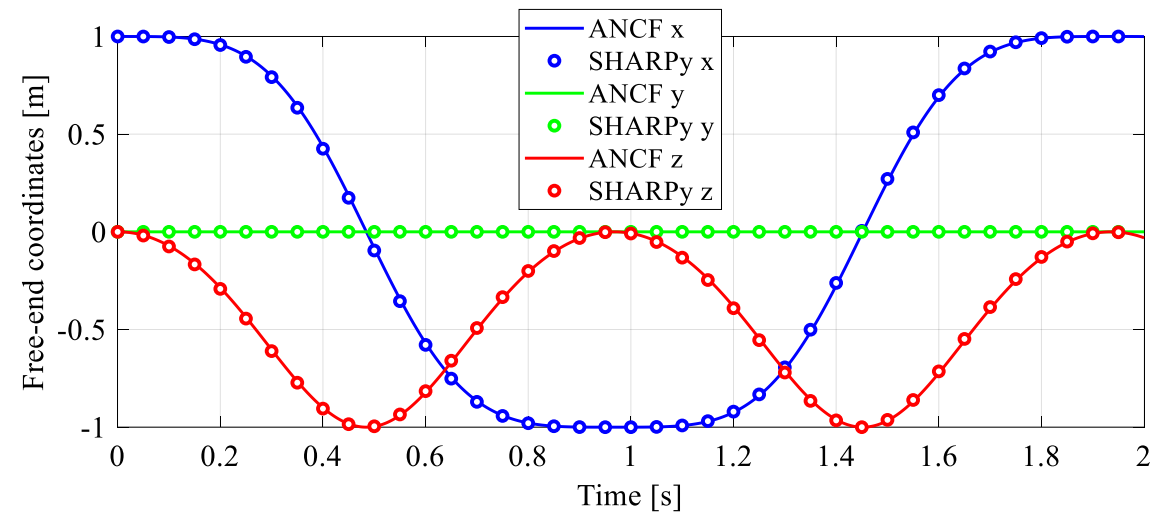


Figure 9 – Time histories of free-end coordinates (c = 1,  $\beta$  = 90).

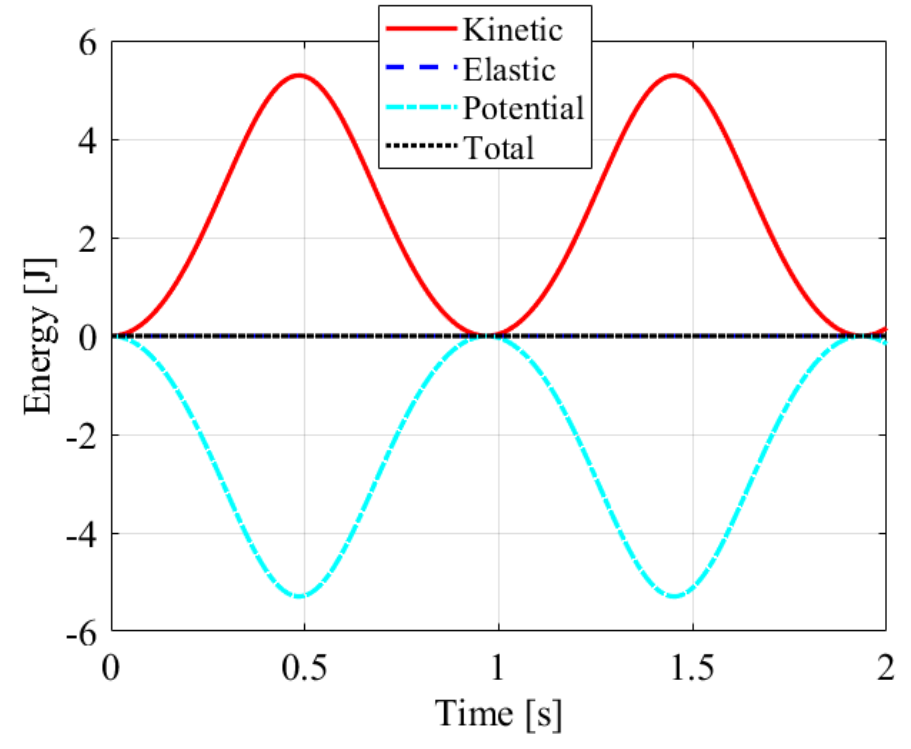


Figure 10 – Time histories of energies of double pendulum calculated by ANCF (c = 1,  $\beta = 90$ ).

# 5.3 c = 1 and $\beta = 45$

Figure 11 shows the X, Y, and Z coordinates at the free end when c=1 and  $\beta=45$ . Because  $\beta=45$ , the Y coordinate is not zero. Even if such 3D motion is caused by the slanted hinge joint, ANCF and SHARPy are in good agreement in the simulation. Owing to this 3D motion, the X and Z coordinates in Fig. 11 are not smooth compared with those in Fig. 9. Figure 12 shows the time histories of the energies calculated by ANCF. The total energy is conserved correctly even when 3D motion is caused by the slanted hinge joint.

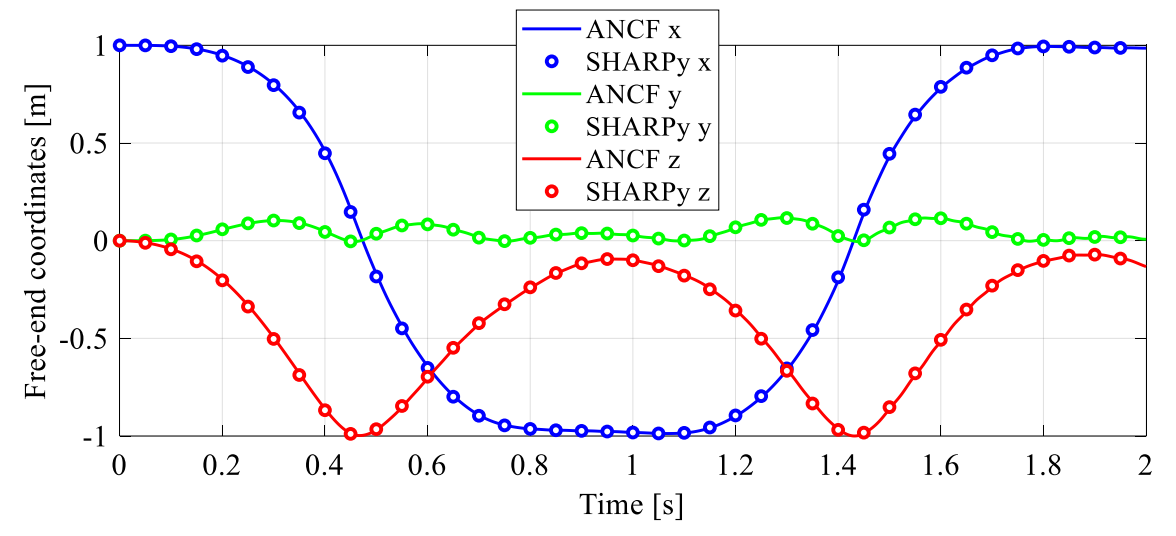


Figure 11 – Time histories of free-end coordinates (c = 1,  $\beta$  = 45).

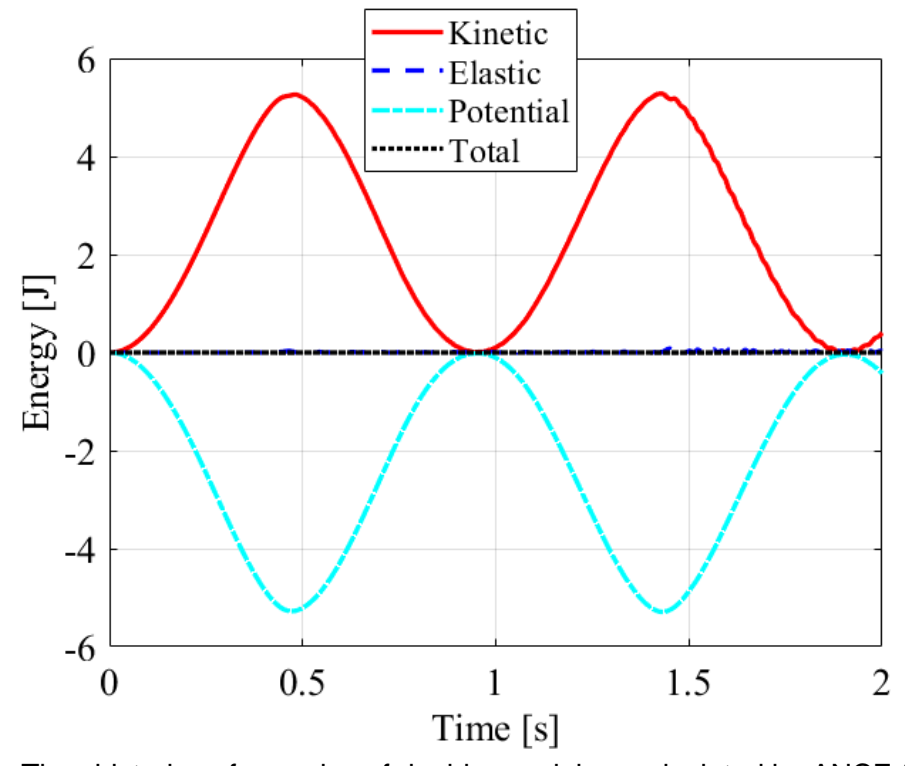


Figure 12 – Time histories of energies of double pendulum calculated by ANCF (c = 1,  $\beta = 45$ ).

# 5.4 c = 0.1 and $\beta = 45$

Figure 13 shows the X, Y, and Z coordinates at the free end when c = 0.1 and  $\beta = 45$ . Because the stiffness decreases, the motion includes higher frequencies attributed to the elastic deformation. ANCF and SHARPy are in good agreement in the simulation when the elastic deformation and slanted hinge joint need to be considered simultaneously. Figure 14 shows the time histories of the energies calculated by ANCF. The total energy is conserved correctly even when the elastic deformation and the slanted hinge joint need to be considered. The elastic energy in this figure is not small compared with those in the simulations with a higher stiffness c = 1.

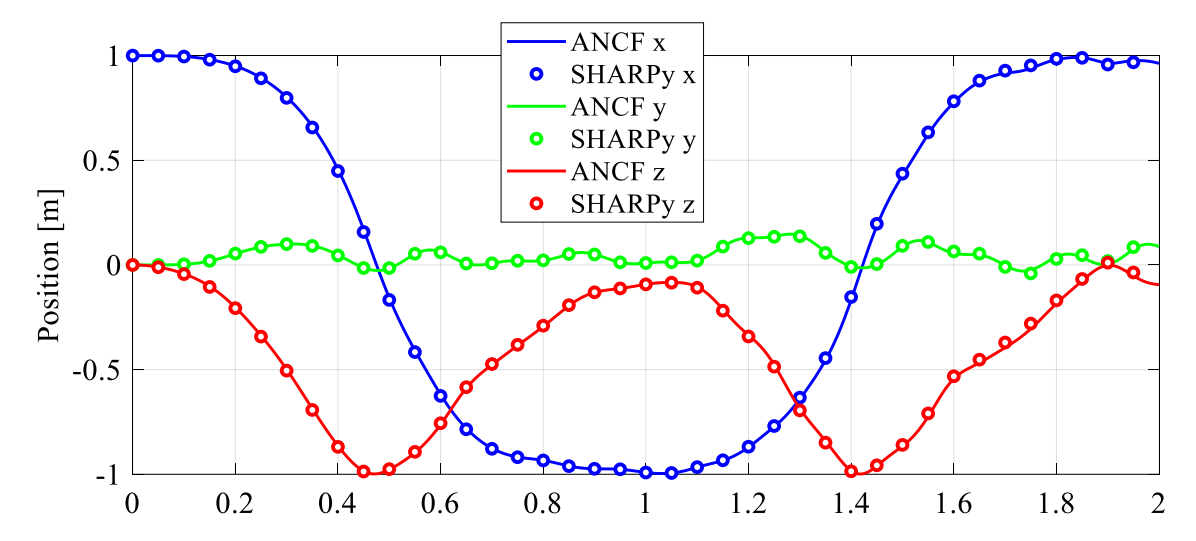


Figure 13 – Time histories of free-end coordinates (c = 0.1,  $\beta$  = 45).

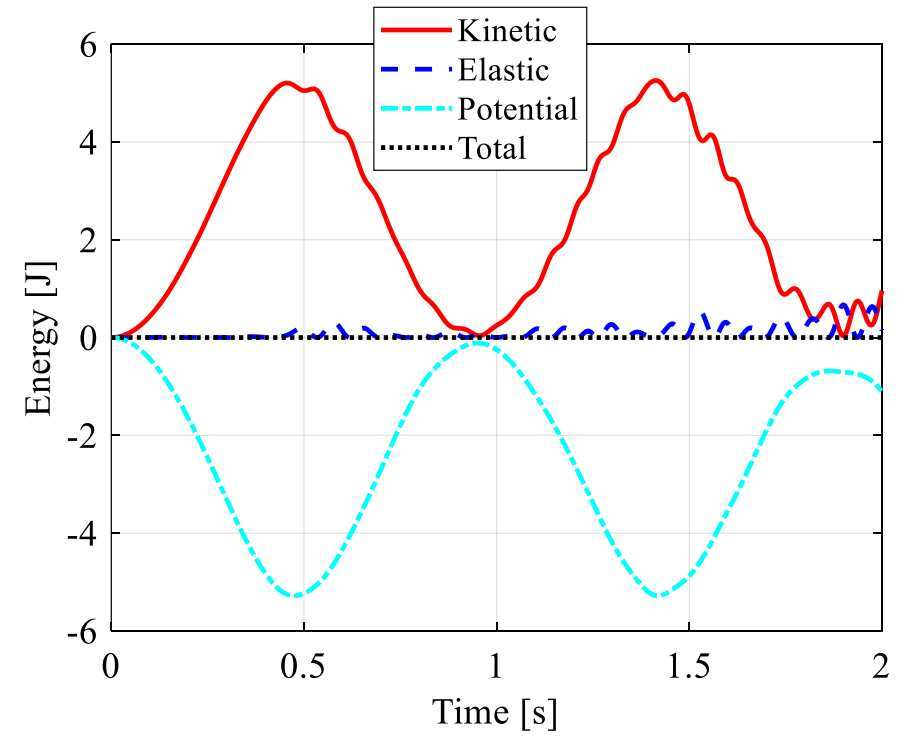


Figure 14 – Time histories of energies of double pendulum calculated by ANCF (c = 0.1,  $\beta = 45$ ).

# 5.5 c = 0.01 and $\beta = 45$

Figure 15 shows the X, Y, and Z coordinates at the free end when c = 0.01 and  $\beta = 45$ . Because the stiffness decreases furthermore, larger elastic deformation occurs. This larger elastic deformation increases the amplitude of the Y coordinate. ANCF and SHARPy are in good agreement in the simulation when the larger elastic deformation occurs. Figure 16 shows the time histories of the energies calculated by ANCF. The total energy is conserved correctly even when the larger elastic deformation occurs. The maximum elastic energy in this figure is larger than those in Figs. 12 and 14.

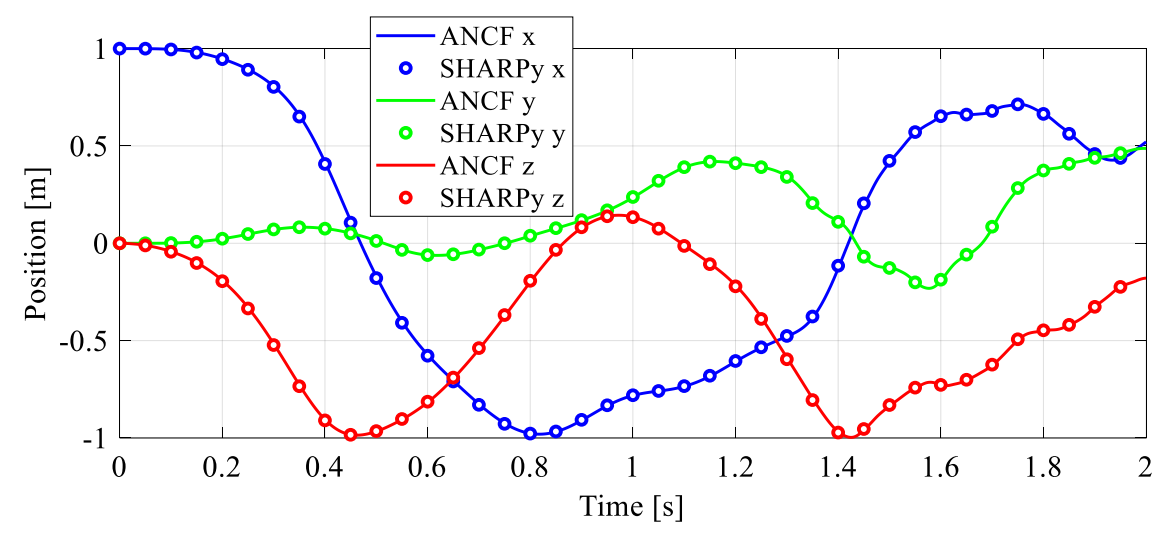


Figure 15 – Time histories of free-end coordinates (c = 0.01,  $\beta$  = 45).

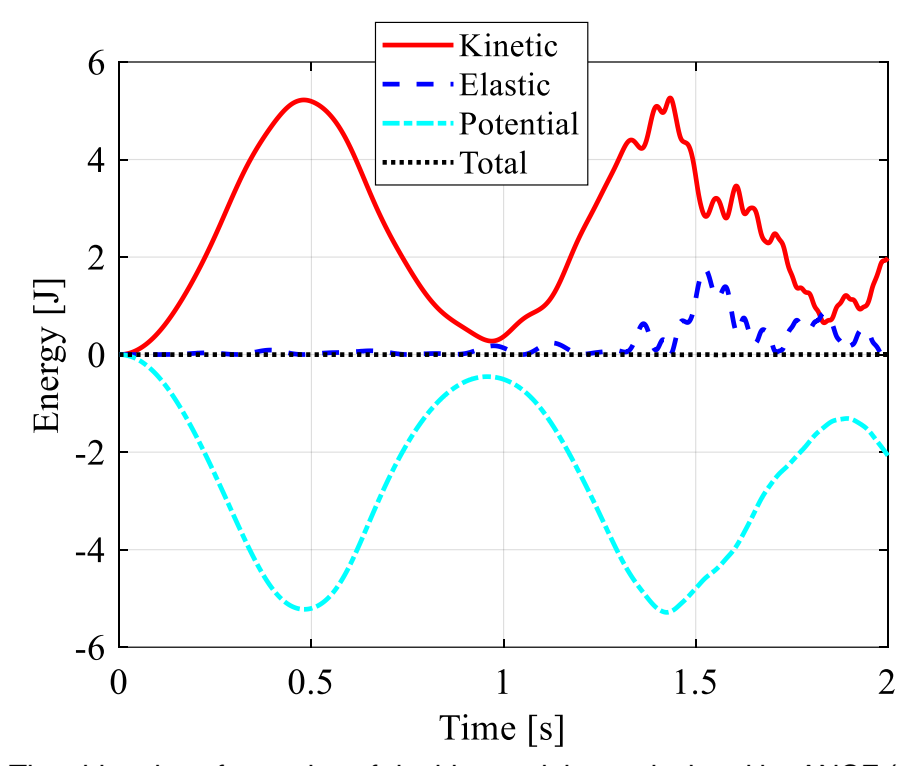


Figure 16 – Time histories of energies of double pendulum calculated by ANCF (c = 0.01,  $\beta$  = 45).

### 6. Aeroelastic Simulation Results of Flared Hinged Wing Assembly

In this section, aeroelastic simulations are performed for a flared hinged wing. The flared hinged wing specifications are based on the high aspect ratio wing with a total wingspan of 16 m [23]. Figure 17 shows the top view of the wing. One end of the wing is fixed to the origin of the global coordinate system. The hinge divides the wing into inner and outer wing bodies. Table 3 shows the specifications of the wing. Table 4 shows the simulation parameters. It should be note that one ANCF element has two nodes, while one GEBF element in SHARPy has three nodes. It should be also noted that finer UVLM panel discretization and smaller time step may result in more converged solutions.

To provide relatively simple validation results, we simulated the transient response caused by the flow that starts to income in the negative Y direction and the gravity that starts to act at t = 0 suddenly. Figure 18 shows the time history of the Z coordinate at the wingtip and the folding angle when AoA is 5 deg and 10 deg. The results of the ANCF simulation framework are in good agreement of those of SHARPy.

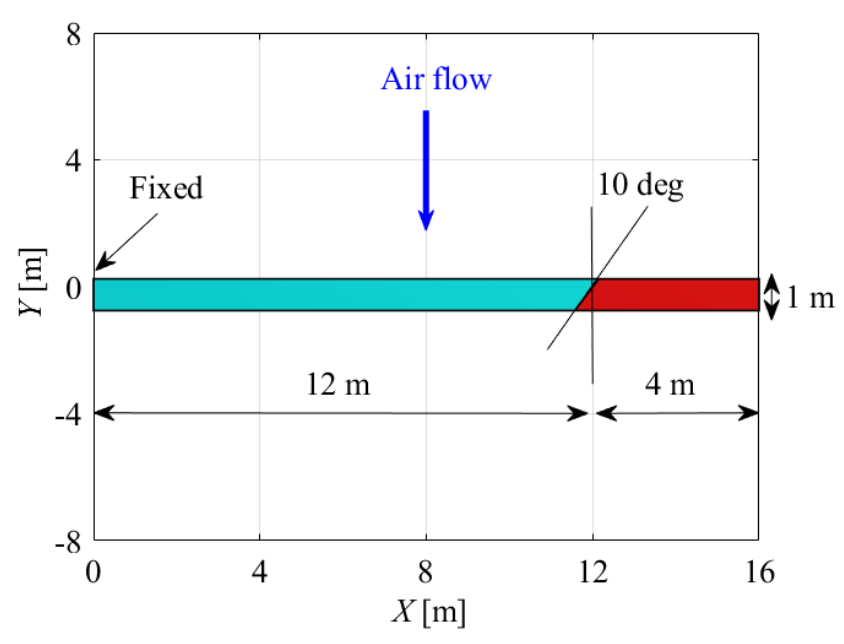


Figure 17 – Top view of flared hinge wing.

Table 3 Parameters of flared hinge wing

Parameters	Symbols	Values	Units
Total length (semispan)	L	16	m
Inner wing length	<i>L</i> <sub>1</sub>	12	m
Outer wing length	$L_2$	4	m
Chord length	С	1	m
Linear density	ρΑ	0.75	kg/m
Rotational inertia around x axis	$ ho I_{xx}$	0.1	kg × m
Rotational inertia around y axis	$ ho I_{yy}$	0.01	kg × m
Rotational inertia around z axis	$ ho l_{zz}$	0.09	kg × m
Extensional stiffness	EA	$1 \times 10^7$	N
Torsional stiffness	GJ	$1 \times 10^4$	$N \times m^2$
Bending stiffness around y axis	$EI_{yy}$	$2 \times 10^{4}$	$N \times m^2$
Bending stiffness around z axis	$EI_{zz}$	$5 \times 10^{6}$	$N \times m^2$
Shear stiffness	GA	$5 \times 10^{6}$	$N \times m^2$

Table 4 Parameters of simulation

Parameters	Symbols	Values	Units	
Simulation time	<i>t</i> end	20	S	
Time step	dt	0.01	S	
Gravity constant	g	9.8	m/s²	
Air density	$ ho_{a}$	0.0889	kg/m³	
Air flow speed	U	25	m/s	
Angle of attack	AoA	0 or 5 or 10	deg	
Flared angle	β	10	deg	
Time integration method	Implicit generalized-α method			
Number of finite element nodes per body	13 for inner wing and 5 for outer wing			
Number of spanwise panels	24 for inner wing and 8 for outer wing			
Number of chordwise panels	4 for inner and outer wing			
Number of streamwise wake panels	40			

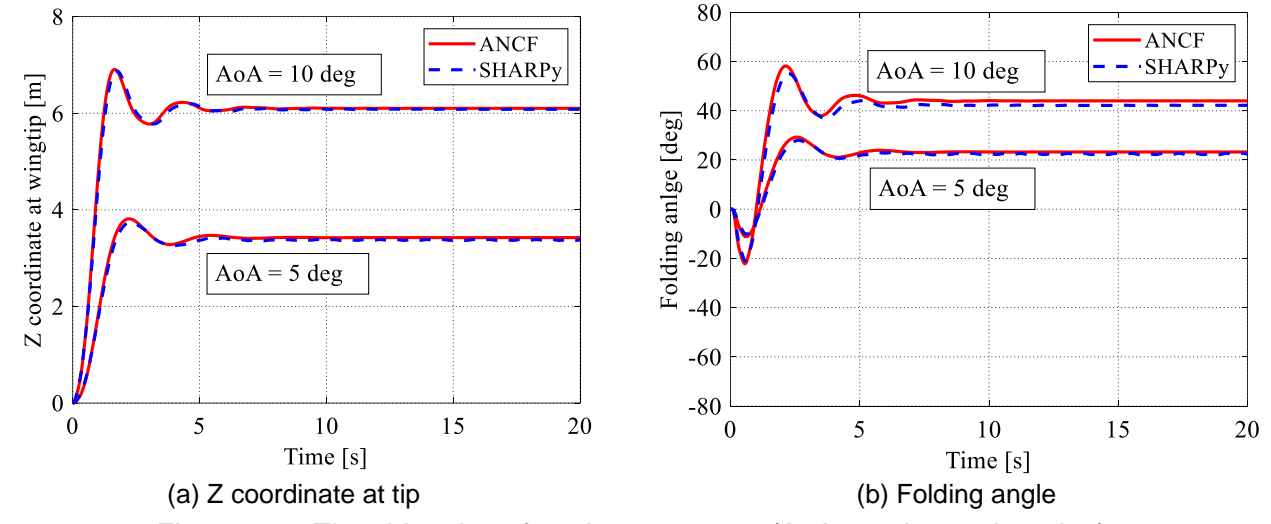


Figure 18 – Time histories of trasient response (AoA = 5 deg and 10 deg).

#### 7. Conclusions

In this paper, the ANCF simulation framework that can consider the slanted hinge joint was developed. Although the past studies demonstrated that the convergence performance of ANCF tends to be inferior to that of GEBF, ANCF enables us to describe the constraint equation for the slanted hinge joint in a simple linear form. Therefore, ANCF can be considered as one of the options suitable for the high aspect ratio wings with slanted hinge joints.

In the free-falling simulations of the double pendulum with a slanted hinge joint, the results of the ANCF simulation framework ware in good agreement with those of SHARPy with GEBF. In the aeroelastic simulations of the high aspect ratio wing with a slanted hinge joint, they were in good agreement. These simulation results would be useful for validating other simulation frameworks for the wing with a slanted hinge joint.

#### 8. Contact Author Email Address

mailto: keisuke.otsuka.d6@tohoku.ac.jp

# 9. Copyright Statement

The authors confirm that they, and/or their company or organization, hold copyright on all of the original material included in this paper. The authors also confirm that they have obtained permission, from the copyright holder of any third party material included in this paper, to publish it as part of their paper. The authors confirm that they give permission, or have obtained permission from the copyright holder of this paper, for the publication and distribution of this paper as part of the ICAS proceedings or as individual off-prints from the proceedings.

# **Acknowledgments**

This work was supported by the Japan Society for the Promotion of Science KAKENHI (grant number 24K17440) and the Nohmura Foundation for Membrane Structure's Technology. Kelvin Chi-Wing Cheng is recipient of an Industrial Cooperative Award in Science and Technology [EP/W522004/1] between the UK Engineering and Physical Sciences Research Council and Airbus UK.

#### References

- [1] Healy F, Cheung R, Rezgui D, Wilson T and Castrichini A. On the effect of geometric nonlinearity on the dynamics of flared folding wingtips. *Journal of Aircraft*, Vol. 60, No. 2, pp 368-381,2023.
- [2] Castrichini A, Cooper J. E, Wilson T, Carrella A and Lemmens Y. Nonlinear negative stiffness wingtip spring device for gust loads alleviation. *Journal of Aircraft*, Vol. 54, No. 2, pp 627-641,2017.
- [3] Palacios R and Cesnik C. E. S. Dynamics of flexible aircraft, Cambridge university press, 2023.
- [4] Cheng C. W, Cea A, Palacios R, Castrichini A and Wilson T. Nonlinear multibody modeling of flexible aircraft with flared hinged wings. *AIAA SciTech 2024 Forum*, Orland FL, AIAA2024-1441, 2024.
- [5] Cesnik C and Brown E. *Modeling of high aspect ratio active flexible wings for roll control.* 43rd AIAA/ASME/ASCE/AHS/ASC Structures, Structural Dynamics, and Materials Conference, Denver, Colorado, AIAA Paper 2002-1719, 2002.
- [6] Sanghi D, Riso C, Cesnik C. E. S and Vetrano, F. Impact of control-surface flexibility on the dynamic response of flexible aircraft, AIAA SciTech 2020 Forum, Orland FL, AIAA 2020-1185, 2020.
- [7] Hodges D. H. Geometrically exact, intrinsic theory for dynamics of curved and twisted anisotropic beams, *AIAA Journal*, Vol. 41, No. 6, pp 1131-1137,2003.
- [8] Wang Y and Otsuka K. Multibody constraints in the geometrically nonlinear intrinsic formulation, *Journal of Computational Nonlinear Dynamics*, Vol. 18, No. 12, p. 121007, 2023.
- [9] Otsuka K. Wang Y. Fujita K. Nagai H and Makihara K. Multifidelity modeling of deployable wings: multibody dynamic simulation and wind tunnel experiment, AIAA Journal, Vol. 57, No. 10, pp 4300-4311, 2019.
- [10]Otsuka K. Wang Y and Makihara K. Versatile absolute nodal coordinate formulation model for dynamic folding wing deployment and flutter analyses, *Journal of Vibration and Acoustics*, Vol. 141, No. 1, p. 011014, 2019.
- [11] Shabana A. A. Dynamics of multibody systems, Cambridge university press, 2020.
- [12] Gerstmayr J. Sugiyama H and Mikkola A. Review on the absolute nodal coordinate formulation for large deformation analysis of multibody systems, *Journal of Computational Nonlinear Dynamics*, Vol. 8, No. 3, p. 031016, 2013.
- [13]Otsuka K, Makihara K and Sugiyama H, Recent advances in the absolute nodal coordinate formulation: literature review from 2012 to 2020, *Journal of Computational Nonlinear Dynamics*, Vol. 17, No. 8, p. 080803, 2022.
- [14]Bauchau O. A, Han S, Mikkola A and Matikainen M. K. Comparison of the absolute nodal coordinate and geometrically exact formulations for beams, *Multibody System Dynamics*, Vol. 32, No. 1, pp. 67-85, 2014.
- [15]Otsuka K, Wang Y and Makihara K, Three-Dimensional Aeroelastic Model for Successive Analyses of High-Aspect-Ratio Wings, *Journal of Vibration and Acoustics*, Vol. 143, No. 6, p. 061006, 2022.
- [16] Murua J, Palacios R and Graham J. M. R. Applications of the unsteady vortex-lattice method in aircraft aeroelasticity and flight dynamics, *Progress in Aerospace Sciences*, Vol. 55, pp. 46-72, 2012.
- [17] Düssler S and Palacios R. Enhanced unsteady vortex lattice aerodynamics for nonlinear flexible aircraft dynamic simulation, *AIAA Journal*, Vol. 62, No. 3, pp 1179-1194, 2024.
- [18]Dong S, Otsuka K and Makihara K, Hamiltonian Formulation with Reduced Variables for Flexible Multibody Systems Under Linear Constraints: Theory and Experiment, *Journal of Sound and Vibration*, Vol. 547, p. 117535, 2023.
- [19]Otsuka K and Makihara K. Absolute nodal coordinate beam element for modeling flexible and deployable aerospace structures, *AIAA Journal*, Vol. 57, No. 3, pp 1343-1346, 2019.
- [20]Del Carre A, Muñoz-Simón A, Goizueta N and Palacios R. SHARPy: A dynamic aeroelastic simulation toolbox for very flexible aircraft and wind turbines. *Journal of Open Source Software*, Vol. 4, No. 44, p. 1885, 2019.
- [21]Muñoz-Simón A. SHARPy: Vortex-lattice-based nonlinear aeroservoelastic modelling and analysis of large floating wind turbines. *Imperial College London PhD Thesis*, 2021.
- [22] Bauchau O. A. Flexible multibody dynamics, Springer, 2011.
- [23] Patil M. J, Hodges D. H and Cesnik C. E. S. Nonlinear Aeroelasticity and Flight Dynamics of High-Altitude Long-Endurance Aircraft, *Journal of Aircraft*, Vol. 38, No. 1, pp. 88-94, 2001.